

Asteroseismology and Dynamics Reveal Interior Structure and Coeval Evolution in the Triply Post-Main-Sequence system DG Leo

PING LI,^{1,2} WEN-PING LIAO*,^{1,2} SHENG-BANG QIAN,³ LI-YING ZHU,^{1,2} JIA ZHANG,¹ QI-BIN SUN,³ AND FANG-BIN MENG^{1,2}

¹ Yunnan Observatories, Chinese Academy of Sciences (CAS), 650216 Kunming, China

² University of Chinese Academy of Sciences, No.1 Yanqihu East Rd, Huairou District, Beijing, China 101408

³ School of Physics and Astronomy, Yunnan University, Kunming 650091, China

ABSTRACT

δ Scuti stars in binary or multiple systems serve as crucial probes for studying stellar pulsation and evolution. However, many such systems are not ideal for asteroseismology due to uncertainties in mass transfer with close companions and the challenges of dynamically measuring all components' physical properties. The triple system DG Leo, comprising an inner binary and a distant δ Scuti star, is an ideal target due to its well-separated pulsator. By combining new *TESS* photometry with archival spectroscopy, our dynamical analysis shows that the system's three components share similar masses, radii, and luminosities within errors, occupying coincident Hertzsprung–Russell diagram positions, indicative of coeval evolution. By fitting seven observed δ Scuti frequencies through asteroseismic modeling with dynamically constrained theoretical grids, we simultaneously trace the pulsating star's evolution and constrain the triple system's evolutionary stage, with the derived fundamental parameters showing consistency with the dynamical solutions. Our analysis reveals that all three components of DG Leo are in the post-main-sequence phase, with a system age of $0.7664^{+0.1402}_{-0.1258}$ Gyr. Additionally, the δ Scuti component shows multiple non-radial modes with significant mixed-character frequencies, providing precise constraints on its convective core extent ($R_{\text{cz}}/R = 0.0562^{+0.0137}_{-0.0021}$).

Keywords: Asteroseismology (73); Stellar oscillations (1617); Delta Scuti variable stars (370); Trinary stars (1714)

1. INTRODUCTION

Systems hosting pulsating stars in binary or multiple configurations provide crucial laboratories for probing stellar deep structure and evolution. Recently, space missions, notably *Kepler* (Borucki et al. 2010) and *TESS* (Ricker et al. 2015), supply high-precision, long-baseline photometry for such systems. Moreover, the spectroscopic data from facilities like *LAMOST* enable determinations of component parameters including mass ratio, effective temperature, chemical composition, and surface gravity. Consequently, fundamental stellar parameters (e.g., mass, radius, luminosity) can be dynamically measured with sufficient accuracy to directly constrain stellar evolution models for pulsators.

δ Scuti stars are A/F-type pulsators located at the intersection of the main sequence and the Cepheid instability strip in the Hertzsprung-Russell (H-R) diagram. Their oscillation periods typically range from 0.02 to 0.25 days (Breger 2000) and are primarily driven by the κ mechanism operating in the helium second ionization zone (Zhevakin 1963; Baker & Kippenhahn 1965; Li & Stix 1994; Chevalier 1971). These stars exhibit both radial and non-radial pulsation modes, making them prime targets for asteroseismic investigations. Furthermore, a subset known as high-amplitude δ Scuti stars (HADS) displays fewer radial modes with high amplitudes, manifesting as single-periodic variations in the radial fundamental or first overtone, as well as double- or triple-periodic pulsations (Netzel & Smolec 2022). Many binary or multiple systems hosting δ Scuti stars are presented (Liakos et al. 2012; Qian et al. 2018; Shi et al. 2022; Chen

Corresponding author: Wen-Ping Liao

*liaowp@ynao.ac.cn

et al. 2022). For example, systems such as HZ Dra (Li et al. 2024), HL Dra (Shi et al. 2021) and CZ Aqr (Zeng et al. 2024) have been reported to have a tertiary star around the inner close binary system. However, many of them are not ideal objects for probing stellar evolution using asteroseismology due to: i) uncertain mass transfer between the δ Scuti component and its close companions (Chen et al. 2020); ii) observational challenges in dynamically determining all components' physical properties via combined spectroscopy, photometry, or astrometry.

DG Leo (TIC 88024537) is a hierarchical and spectroscopic triple system consisting of a inner binary (components Aa and Ab) and a distant companion (component B) forming a wider visual binary. The close binary components both exhibit spectral types A8 IV (Hoffleit & Jaschek 1982), while the composite spectrum has been classified as F0 IIIIn (Cowley 1976) and A7 III (Cowley & Bidelman 1979). The orbital period of the Aa,b system is 4.147 days (Fekel & Bopp 1977), while the orbital period of the visual pair A & B is approximately 200 years. The visual component B, observed by *Hipparcos* with an angular separation of $0''.17$ and a magnitude difference of 0.69 mag relative to Aa,b (ESA 1997), was monitored through micrometric observations and speckle interferometry from 1935 to 1997 (Hartkopf et al. 2000). Existing astrometric data indicate a highly inclined and potentially eccentric orbit. Previous studies (Barnes et al. 1977; Rosvick & Scarfe 1991a) presented evidence for possible shallow eclipses with an inclination of $\sim 75^\circ$ for the Aa,b system.

All three components of this system reside within the δ Scuti instability strip, rendering them potential pulsators. Danziger & Dickens (1967) first reported short-period variability in the system but could not determine its nature. Furthermore, claims regarding short-period oscillations primarily concern component B, which is classified as both an ultra-short-period Cepheid (Eggen 1979) and a δ Scuti star (Elliott 1974), with possible changes in amplitude and phase reported by Antonello & Mantegazza (1982); Rosvick & Scarfe (1991b). Two decades ago, the spectroscopic analysis resolved this ambiguity: the inner binary consists of two Am stars, at least one rotating asynchronously despite a circular orbit, whereas component B is a chemically normal δ Scuti pulsator (Frémat et al. 2005). Ellipsoidal variations from tidally deformed components were first detected by Lampens et al. (2004, 2005).

In summary, despite extensive studies on DG Leo, key physical properties such as masses of its three component stars remain undetermined dynamically. Recently, the *TESS* mission observed DG Leo across four sectors (Sectors 21, 45, 46, and 72), providing continuous 120-second cadence light curves (All of the *TESS* data used in this paper can be found through the MAST: doi:10.17909/k0fp-8v04). When combined with the spectroscopic results of previous studies (Lampens et al. 2004, 2005), this provides a unique opportunity to determine the physical parameters (e.g., mass, radius) of all three components dynamically. It is then possible to infer the evolution of the triple system by investigating the component B using asteroseismology. This also enables us to probe the interior structure of component B. Thanks to its clear separation and these sufficient observations, DG Leo is therefore a good target for studying stellar evolution using asteroseismology.

The paper is structured as follows. Section 2 details the modeling of the *TESS* light curve and derivation of stellar parameters. Section 3 presents the analysis of pulsational characteristics in DG Leo. In Section 4, we describe the construction and analysis of the stellar model for DG Leo. Finally, Section 5 provides the main discussions and conclusions.

2. MODELING THE INNER BINARY SYSTEM

As shown in the top and second panels of Figure 1, the ellipsoidal variations reported by Lampens et al. (2004, 2005) are also present in the *TESS* light curve. The dominant period of 2.0737 d corresponds to half the orbital period of the inner spectroscopic binary. However, the signal with period of 4.166 d (Lampens et al. 2004) is not determined in the *TESS* light curve. Moreover, as shown in the bottom panel of Figure 1, the peak pulsation amplitude is about 0.01 mag. This is an order of magnitude smaller than the typical amplitude of HADS stars, which are defined by V-band variations exceeding 0.1 mag (Templeton et al. 2002).

To derive reliable orbital parameters for this inner binary system, we modeled the light curves of four sectors using the Wilson–Devinney (W-D) method (Wilson & Devinney 1971; Wilson 1979, 1990; Van Hamme & Wilson 2007; Wilson 2012). To minimize the influence of pulsation effects and enhance the data reliability, we generated an averaged light curve through a two-step process: (i) converting TJD values to phase units, and (ii) reducing the original dataset from over 18,998 data points to 200 representative points by averaging within each sector. Specifically, all points falling within a phase interval of 0.005 were combined into a single averaged point, thereby smoothing the curve while preserving key features.

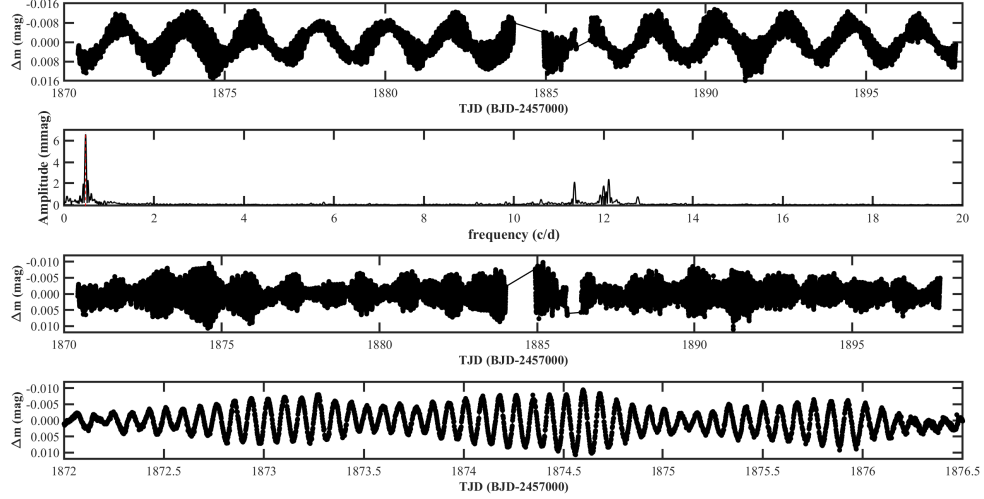


Figure 1. The *TESS* light curve and corresponding Fourier amplitude spectrum of DG Leo. Top panel: the full light curve from Sector 21. Second panel: the Fourier amplitude spectrum derived from the full light curve. The dominant frequency peak at 0.4822 d^{-1} (red dashed vertical line) corresponds to ellipsoidal variations, while other significant peaks represent pulsation frequencies. Third panel: the light curve after removing the dominant ellipsoidal variations. Bottom panel: a zoomed-in view of the detrended light curve between TJD 1872–1876.5. (TJD = BJD – 2457000.0).

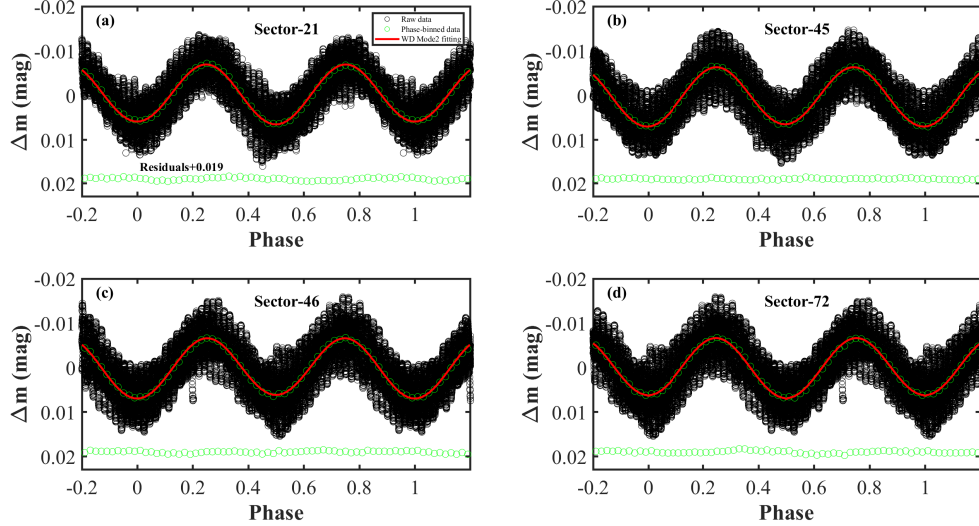


Figure 2. The light curves from four *TESS* sectors and their corresponding phase-binned light curves (green circles) are overplotted with the best-fitting model (red solid curves; W-D Model 2). Residuals are shown in the bottom panel for each sector.

Prior to light curve modeling, important parameters were fixed in the W-D code, with the primary star's effective temperature set to $7470 \pm 220 \text{ K}$ (Frémat et al. 2005, 2004). As both components are early-type stars, their bolometric albedos A_1 and A_2 were fixed at 1.00 (Claret 2001) and gravity-darkening coefficients g_1 and g_2 at 1.00 (Lucy 1967), while the mass ratio $q = M_2/M_1$ was fixed at the spectroscopic value 1.000 ± 0.001 (Frémat et al. 2005, 2004). Linear limb-darkening coefficients x_1 and x_2 were adopted from Van Hamme (1993). For the inner binary system, W-D Model 2 (detached configuration) was implemented, with orbital eccentricity and period fixed at $e = 0$ and $P = 4.146751 \text{ d}$ respectively (Frémat et al. 2005), while free parameters—including primary luminosity (L_1), orbital

Table 1. Light curve modeling solutions for four sector light curves of DG Leo. The numbers in brackets are the errors in the last two bits of the data. The units of most parameters are dimensionless, except for those explicitly specified.

Parameters	Sector 21	Sector 45	Sector 46	Sector 72	Mean values
Period (d)	4.146751	4.146751	4.146751	4.146751	4.146751
i ($^{\circ}$)	66.55(95)	66.0(13)	66.0(18)	68.91(48)	66.87(60)
q (M_2/M_1)	1.000	1.000	1.000	1.000	1.000
T_1 (K)	7470	7470	7470	7470	7470
T_2/T_1	0.9705(53)	0.9683(55)	0.1024(41)	1.030(48)	0.998(17)
$L_1/(L_1 + L_2)_{\text{TESS}}$	0.5286(46)	0.5242(39)	0.486(31)	0.523(33)	0.515(10)
$L_2/(L_1 + L_2)_{\text{TESS}}$	0.4714(46)	0.4758(39)	0.514(31)	0.477(33)	0.485(10)
Ω_1	6.192(38)	6.415(51)	6.41(17)	6.29(12)	6.327(53)
Ω_2	5.28(41)	6.434(40)	6.43(20)	6.76(33)	6.226(325)
$r_1(\text{pole})^b$	0.1834(28)	0.1841(17)	0.1841(58)	0.1884(41)	0.185(1)
$r_1(\text{point})^b$	0.1859(32)	0.1874(18)	0.1874(62)	0.1920(44)	0.188(1)
$r_1(\text{side})^b$	0.1844(29)	0.1853(18)	0.1853(59)	0.1897(42)	0.186(1)
$r_1(\text{back})^b$	0.1855(31)	0.1869(18)	0.1869(61)	0.1915(44)	0.188(1)
$r_2(\text{pole})^b$	0.180(23)	0.1834(33)	0.1835(66)	0.1733(98)	0.180(2)
$r_2(\text{point})^b$	0.184(25)	0.1866(75)	0.1867(71)	0.176(10)	0.183(3)
$r_2(\text{side})^b$	0.181(23)	0.1846(30)	0.1846(68)	0.174(10)	0.181(2)
$r_2(\text{back})^b$	0.183(25)	0.1862(45)	0.1862(70)	0.175(10)	0.183(3)
f_1 (Filling degree of the primary)	0.0952(75)	0.1173(18)	0.1173(59)	0.1259(44)	0.114(7)
f_2 (Filling degree of the second)	0.134(29)	0.1160(21)	0.1160(67)	0.0974(89)	0.116(7)
Absolute parameters					
M_1 (M_{\odot})	2.258(33)		M_B (M_{\odot})	2.39(40)	
M_2 (M_{\odot})	2.258(33)			
R_1 (R_{\odot})	3.353(15)		R_B (R_{\odot})	2.95(50)	
R_2 (R_{\odot})	3.263(25)			
L_1 (L_{\odot})	25.99(1.44)		L_B (L_{\odot})	26.05(8.42)	
L_2 (L_{\odot})	24.48(1.67)			
a (R_{\odot})	17.955(62)			

^b In units of semi-major axis.

inclination (i), primary potential (Ω_1), secondary potential (Ω_2), and secondary temperature (T_2)—were iteratively adjusted during optimization.

These free parameters were iteratively adjusted until achieving converged solutions. The results for all four sectors’ light curves are listed in the second, third, fourth, and fifth columns of Table 1. Based on these solutions, theoretical light curves were calculated as depicted by the red curves in Figure 2. The light-curve residuals for each solution are plotted in the bottom panel for each sector (green circles). All four converged solutions reveal that the inner binary of DG Leo is a detached system consisting of two A-type components with low Roche lobe filling factors.

Combining the spectroscopic solution (Lampens et al. 2004; Frémat et al. 2005) with the mean values of the light-curve modeling results, we dynamically determined the physical parameters (e.g, mass, radius, luminosity, and separation) of both components as listed in Table 1. Based on the mass ratio of 0.374 ± 0.046 between the distant component B and the total system mass—determined by Frémat et al. (2005), we calculated the mass of component B and included it in Table 1. Additionally, we estimated the radius and luminosity of component B, with the radius agreeing well with $R_B = 2.99 \pm 0.20 R_{\odot}$ from Frémat et al. (2005).

3. FREQUENCY ANALYSIS

TESS observed DG Leo continuously from TJD 2526.0097 to TJD 2578.7048, generating data files s45–s46. To analyse the pulsation properties of DG Leo, we subtracted the light curve model from these *TESS* light curves. The frequency resolution for this dataset is $\delta f = 1/\Delta T \approx 0.0189$ c/d, where ΔT is the total observational time span for sectors s45–s46. We conducted a detailed analysis for investigating the pulsation features through multiple frequency analysis of the light curve residuals using the *Period04* software (Lenz & Breger 2005). Since no pulsation signals were detected in the high-frequency region ($f > 100$ c/d), subsequent frequency extraction was confined to the range 0–100 c/d.

In each iteration step, we identified the frequency with the highest amplitude and performed a multi-period least-squares fit to the data, incorporating all previously detected frequencies. The data were then pre-whitened using

this solution, and the resulting light curve residuals served as the basis for further analysis. This process continued iteratively until the residuals met the signal-to-noise threshold of $S/N \geq 4.0$ (Breger et al. 1993). Ultimately, a total of 40 frequencies were detected, of which 38 satisfied the $S/N \geq 4.0$ criterion; these are listed in Table 2. Based on the method described by Montgomery & O'Donoghue (1999), we calculate the noise within a 1 c/d bandwidth centered on each frequency. We also determine the corresponding amplitudes and their uncertainties. Figure 3 displays the light curve residuals after the removal of the binary model (blue dots) with the Fourier fit (red curve) and its corresponding Fourier spectrum. The top panel reveals pulsations with a maximum amplitude of 0.010 mag, which is substantially lower than the 0.016 mag amplitude of the ellipsoidal variation that was removed (see top panel of Figure 1).

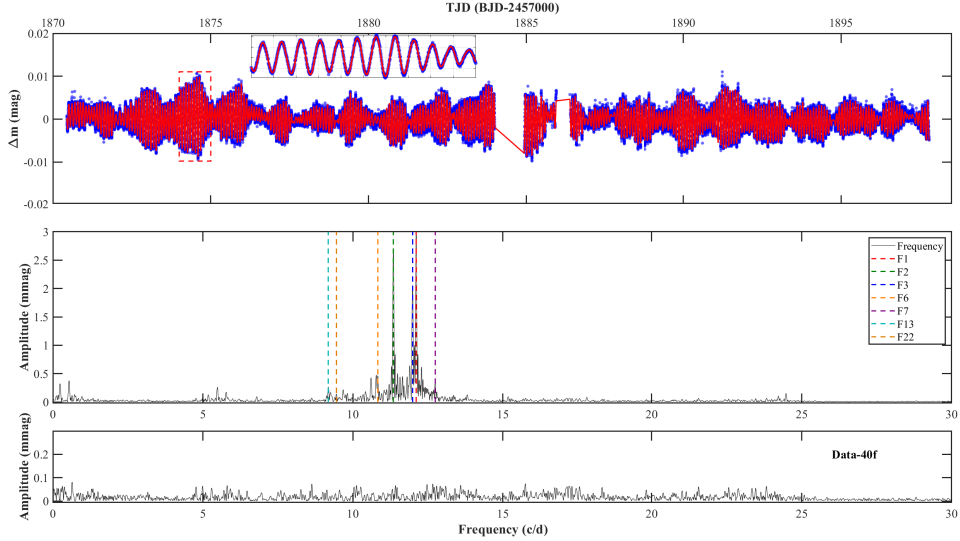


Figure 3. The light curve of DG Leo after subtracting the binary model, along with its corresponding Fourier spectra. Top panel: the residual light curve (blue dots) with the Fourier fit model overplotted (red curve). The inset shows a zoomed-in view of the same light curve between TJD 1872 and 1874. Middle panel: the Fourier amplitude spectrum of the residual light curve; the seven independent frequencies are marked by colored vertical dashed lines. Bottom panel: the residual spectrum after pre-whitening with 40 significant frequencies.

We examined the extracted frequencies to identify linear combination frequencies of the form $F_k = mF_i + nF_j$ (Pápics 2012; Kurtz et al. 2015), where m and n are integers, F_i and F_j represent parent frequencies, F_k denotes the combination frequency. A peak is classified as a combination if it satisfies two criteria: (1) both parent frequencies have amplitudes greater than the presumed combination term, and (2) the difference between observed and predicted frequencies is smaller than the frequency resolution δf (Loumos & Deeming 1978; Lee et al. 2019). As summarized in Table 2, we identified 24 linear combination frequencies, 6 possible side lobe, and one unknown frequency. Moreover, seven independent frequencies were identified: F_1 , F_2 , F_3 , F_6 , F_7 , F_{13} , and F_{22} . These are indicated by the colored vertical dashed lines in Figure 3. The seven independent frequencies range from 9 to 13 c/d (corresponding to periods of 0.07 to 0.1 d). This period range falls well within the typical period range known for δ Scuti stars (e.g., 0.02-0.25 d, Breger (2000)).

For identifying the pulsation modes of the independent frequencies, we calculated the pulsation constant Q values for the 7 independent frequencies using the following basic relation for pulsating stars:

$$Q = P_{\text{osc}} \sqrt{\frac{\bar{\rho}}{\bar{\rho}_{\odot}}}, \quad (1)$$

where P_{osc} is the pulsation period and mean density is $\bar{\rho} = 0.094(\pm 0.011)\bar{\rho}_{\odot}$. The mean density of component B is estimated based on the parameters in Table 1. The values of Q for each frequency are used for comparison with the theoretical models (Fitch 1981) for $M=2.0 M_{\odot}$ and $2.5 M_{\odot}$. The probable l -degrees and the types of each independent frequency are identified and listed in Table 3.

Table 2. Pulsating frequencies of DG Leo. The numbers in parentheses are the errors on the last bit of the data. The seven independent frequencies are indicated by bold formatting. **Frequencies marked as 'Combination' represent higher-order linear combinations of these independent frequencies.**

ID	Freq. (c/d)	Ampl. (mag)	Remark	S/N	ID	Freq. (c/d)	Ampl. (mag)	Remark	S/N
F_1	12.112052 (61)	0.003057 (8)		113.96	F_{20}	11.084639 (100)	0.000186 (8)	Sidelobe	9.05
F_2	11.350499 (70)	0.002667 (8)		143.58	F_{21}	9.820529 (108)	0.000172 (8)	$3F_2 - 2F_1$	8.83
F_3	11.993720 (92)	0.002017 (8)		79.08	F_{22}	9.453882 (115)	0.000161 (8)		7.83
F_4	11.925598 (354)	0.000525 (8)	Sidelobe	21.36	F_{23}	24.475474 (122)	0.000152 (8)	$4F_1 - 2F_3$	9.82
F_5	12.282446 (359)	0.000516 (8)	$2F_1 - F_4$	19.57	F_{24}	9.268517 (126)	0.000147 (8)	Combination	6.99
F_6	10.833761 (432)	0.000430 (8)		19.81	F_{25}	0.110737 (160)	0.000116 (8)	$F_1 - F_3$	4.92
F_7	12.748753 (487)	0.000381 (8)		13.77	F_{26}	13.823227 (153)	0.000121 (8)	Sidelobe	4.94
F_8	0.545826 (58)	0.000322 (8)	Combination	12.39	F_{27}	10.328425 (149)	0.000125 (8)	Combination	6.18
F_9	11.723486 (50)	0.000371 (8)	Combination	16.97	F_{28}	5.184296 (165)	0.000113 (8)	Combination	5.91
F_{10}	10.604561 (52)	0.000358 (8)	$2F_2 - F_1$	17.12	F_{29}	24.225893 (169)	0.000110 (8)	$2F_1$	6.37
F_{11}	10.779992 (47)	0.000396 (8)	Combination	18.50	F_{30}	9.708836 (150)	0.000124 (8)	Sidelobe	6.15
F_{12}	0.236882 (58)	0.000319 (8)	Combination	13.50	F_{31}	0.734395 (10)	0.001872 (8)	Sidelobe	79.97
F_{13}	9.180254 (70)	0.000264 (8)		13.09	F_{32}	15.179588 (185)	0.000100 (8)	Combination	5.47
F_{14}	5.483229 (70)	0.000264 (8)	Combination	12.58	F_{33}	6.796465 (190)	0.000098 (8)	$7F_2 - 6F_1$	5.71
F_{15}	10.424492 (81)	0.000229 (8)	Combination	11.04	F_{34}	0.963339 (187)	0.000099 (8)	Combination	4.60
F_{16}	9.683210 (86)	0.000215 (8)	Combination	10.76	F_{35}	0.735726 (100)	0.001853 (8)	Sidelobe	79.20
F_{17}	5.776923 (95)	0.000196 (8)	Combination	10.07	F_{36}	9.900610 (215)	0.000086 (8)	Combination	4.38
F_{18}	11.277650 (96)	0.000194 (8)	Combination	10.46	F_{37}	0.505719 (119)	0.000155 (8)	unknown	5.99
F_{19}	12.075402 (89)	0.000208 (8)	Combination	8.03	F_{38}	0.639501 (184)	0.000101 (8)	$F_7 - F_1$	4.09

Table 3. The independent pulsating frequencies detected in DG Leo.

ID	F_{obs} (c/d)	$Q \times 100$	l -degrees	Mode
F_1	12.112052 (61)	2.53	0	1H
F_2	11.350499 (70)	2.70	2	NRP1
F_3	11.993720 (92)	2.55	3	NRP1
F_6	10.833761 (432)	2.82	1, 2 or 3	NRP1
F_7	12.748753 (487)	2.40	3	NRP1
F_{13}	9.180254 (70)	3.33	2 or 3	f or g
F_{22}	9.453882 (115)	3.24	0	F

NOTE— The labels denote pulsation modes as follows: F (fundamental radial mode), 1H (first overtone radial mode), NRP1 (non-radial mode with one order), f (f-mode), and g (g-mode).

As shown in Table 3, the values of Q indicate F_1 is a first-overtone radial mode while F_{22} is fundamental. The period ratio between F_1 and F_{22} (0.780) matches the theoretical fundamental/first-overtone value (0.772), confirming F_{22} as the fundamental radial mode and F_1 as the first overtone (Grigahcène et al. 2005; Fitch 1981; Poretti et al. 2005). We identify F_2 as a non-radial mode with $l=2$. Similarly F_3 and F_7 are both found to be non-radial modes with $l=3$. Finally, F_6 and F_{13} are also tentatively classified as non-radial modes, with possible l -values of 1, 2, or 3, though their exact values remain uncertain.

As shown in the top and bottom panels of Figure 1, the high pulsation amplitudes vary with time, suggesting potential modulation with the orbital period of the inner binary. Such variations, which could indicate tidally induced pulsations, have been observed in systems like HD 74423 (Handler et al. 2020), TIC 63328020 (Rappaport et al. 2021), and CO Cam (Kurtz et al. 2020). To investigate this possibility, we analyzed the *TESS* photometry to search for

modulation of the pulsation signals (e.g., frequency splittings, or amplitude and phase variations phased with the orbital period). However, unlike the case of HD 74423, we did not detect any pulsation frequency splitting modulated at the orbital frequency.

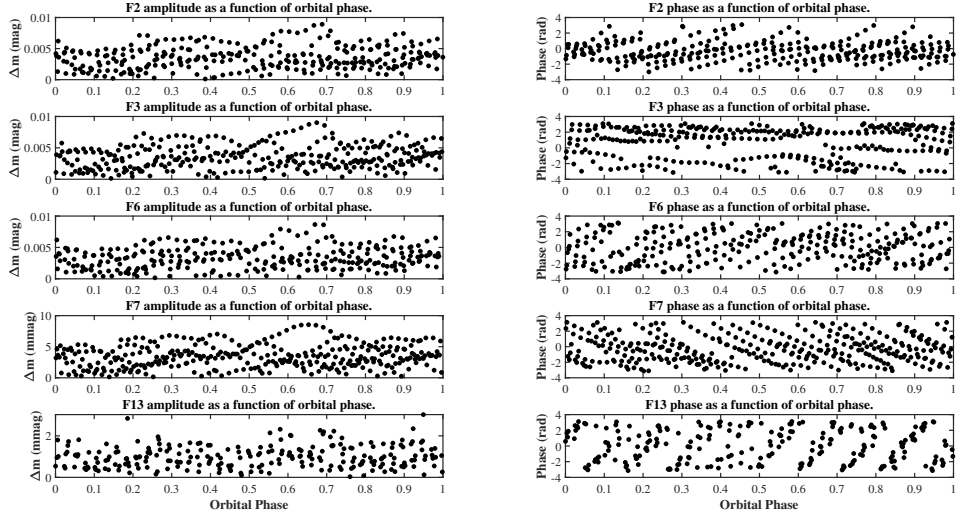


Figure 4. The five non-radial pulsation amplitudes and phases, modulated over the orbital period of the inner binary. The time zero point is set to $t_0 = \text{BJD } 2458871.77213$, chosen such that the phases of the first two orbital sidelobes are equal.

Furthermore, following the method of Handler et al. (2020), we performed a least-squares fit to sections of the data to examine orbital-phase-dependent variations in amplitude and phase for the non-radial modes F_2 , F_3 , F_6 , F_7 , and F_{13} . The data were segmented into intervals of 0.09 d (for F_2 , F_3 , F_6), 0.08 d (for F_7), and 0.10 d (for F_{13}). As shown in Figure 4, no significant amplitude or phase modulation over the orbital cycle of the inner binary was found for these five non-radial pulsation modes. This indicates that the observed pulsations likely originate from component B rather than being tidally modulated by the inner binary, which is consistent with the conclusion of Frémat et al. (2005) that the pulsations arise from component B.

4. STELLAR MODELS

4.1. Input Physics

We thus utilize the stellar evolution code Modules for Experiments in Stellar Astrophysics (MESA, version r22.11.1), developed by Paxton et al. (2011, 2013, 2015, 2018), to compute evolutionary and pulsational models for component B. Specifically, for generating stellar evolution models and calculating the adiabatic frequencies of radial and non-radial modes, we employ the *pulse_adipls* (Christensen-Dalsgaard 2008) submodule in MESA. Our calculations adopt the 2005 update of the OPAL equation of state tables (Rogers & Nayfonov 2002). For opacity, we utilize the OPAL high-temperature tables from Iglesias & Rogers (1996) and the low-temperature tables from Ferguson et al. (2005). We assume the initial metallicity is identical to the solar value (Asplund et al. 2009). Convective zones are treated using the classical mixing-length theory (Böhm-Vitense 1958) with a mixing-length parameter $\alpha = 1.90$ (Paxton et al. 2011).

To model convective core overshooting, we adopt an exponentially decaying prescription for the overshooting - mixing diffusion coefficient (Freytag et al. 1996; Herwig 2000):

$$D_{\text{ov}} = D_0 \exp \left(\frac{-2z}{f_{\text{ov}} H_p} \right), \quad (2)$$

where D_0 is the diffusion coefficient at the edge of the convective core, z is the distance into the radiative zone from the edge, f_{ov} is an adjustable parameter describing the efficiency of overshooting, and H_p is the pressure scale height. The lower limit of the diffusion coefficient is set to $D_{\text{ov}}^{\text{limit}} = 1 \times 10^{-2} \text{ cm}^2 \text{ s}^{-1}$ (Chen et al. 2019), below which overshooting

is neglected in our models. In addition, we do not include elemental diffusion, stellar rotation, and magnetic fields in the stellar structure and evolution calculations.

4.2. Grid of Stellar Models for Component B

Stellar evolution paths and internal structures depend critically on the initial mass M , initial chemical composition (X, Y, Z), and the convective overshooting parameter f_{ov} . Following Li et al. (2018), we adopt the helium abundance relation $Y = 0.249 + 1.33Z$, thereby reducing the number of independent parameters to M, Z , and f_{ov} . We perform a grid search over stellar masses M from 2.00 to 2.30 M_{\odot} with a step of 0.01 M_{\odot} according our results of light curve modeling, and metallicities Z from 0.010 to 0.030 in steps of 0.001. For the overshooting at the top of the convective core, we follow the method of Chen et al. (2019) to take four different cases: no overshooting ($f_{\text{ov}} = 0$), moderate overshooting ($f_{\text{ov}} = 0.01$), intermediate overshooting ($f_{\text{ov}} = 0.02$), and extreme overshooting ($f_{\text{ov}} = 0.03$).

Each star in the grid is computed from the zero-age-main-sequence to the post-main-sequence stage ($X_c = 1 \times 10^{-5}$). The effective temperatures of δ Scuti normally vary between 6000 K and 9800 K (Aerts et al. 2010). we restrict the effective temperature of stellar models inside this range. Luminosity and radius are constrained to $1.24 < \log(L/L_{\odot}) < 1.53$ and $0.39 < \log(R/R_{\odot}) < 0.53$, based on results from our light curve modeling. As a star moves along its evolutionary track into this region, the adiabatic frequencies of the radial ($\ell = 0$) and non-radial ($\ell = 1, 2$, and 3) oscillations are calculated for the structure model at each stage of its evolution.

Additionally, we also include stellar rotation as a fourth adjustable parameter, varying the rotation velocity V_{rot} from 30 to 50 km s⁻¹ in steps of 1 km s⁻¹ due to the component B's project velocity is $v \sin i \geq 30$ km s⁻¹ (Frémat et al. 2005). For each pulsation mode at a given P_{rot} , rotational splitting produces $2l + 1$ frequency components according to:

$$\nu_{l,n,m} = \nu_{l,n} + m\delta\nu_{l,n} = \nu_{l,n} + \beta_{l,n} \frac{m}{P_{\text{rot}}} \quad (3)$$

(Saio 1981; Dziembowski & Goode 1992; Aerts et al. 2010), where $\delta\nu_{l,n}$ is the rotational splitting frequency and $\beta_{l,n}$ determines the splitting magnitude. For uniformly rotating stars, $\beta_{l,n}$ is given by Aerts et al. (2010):

$$\beta_{l,n} = \frac{\int_0^R (\xi_r^2 + L^2\xi_h^2 - 2\xi_r\xi_h - \xi_h^2) r^2 \rho dr}{\int_0^R (\xi_r^2 + L^2\xi_h^2) r^2 \rho dr}, \quad (4)$$

where ξ_r and ξ_h are the radial and horizontal displacement eigenfunctions, ρ is the local density, and $L^2 = l(l+1)$. According to Equation 3, each dipole mode splits into three different components, corresponding to modes with $m = -1, 0$, and $+1$, respectively. Each quadrupole mode splits into five different components, corresponding to modes with $m = -2, -1, 0, +1$, and $+2$, respectively.

4.3. Fitting Results of Component B

Based on the mode identification in section 3, we compare model frequencies with spherical degrees $l = 0, 1, 2$, and 3 to the observed frequencies $F_1, F_2, F_3, F_6, F_7, F_{13}$, and F_{22} to identify the optimal model. The goodness of fit is evaluated using:

$$S^2 = \frac{1}{k} \sum_{i=1}^k |f_{\text{model},i} - f_{\text{obs},i}|^2, \quad (5)$$

where $f_{\text{obs},i}$ is the i -th observed frequency, $f_{\text{model},i}$ is the corresponding model frequency, and k is the number of observed modes. The frequencies F_6 and F_{13} could not be precisely identified in advance; therefore, the nearest theoretical frequencies were assigned to represent them in the model.

Figures 5 and 6 display the variation of the goodness-of-fit S_m^2 across different physical parameters. Each dot in the figures represents one minimum value of S_2 along one evolutionary track, denoted as S_m^2 . Horizontal lines in both figures indicate $S_m^2 = 0.10$, corresponding to the squared value of the frequency resolution δf . Dots above this threshold correspond to 84 candidate models that are listed in Table 6 (see in Appendix). Model A3 achieves the global minimum $S_m^2 = 0.0343$, establishing it as the optimal solution. This best-fitting model is highlighted by red dots in Figures 5 and 6.

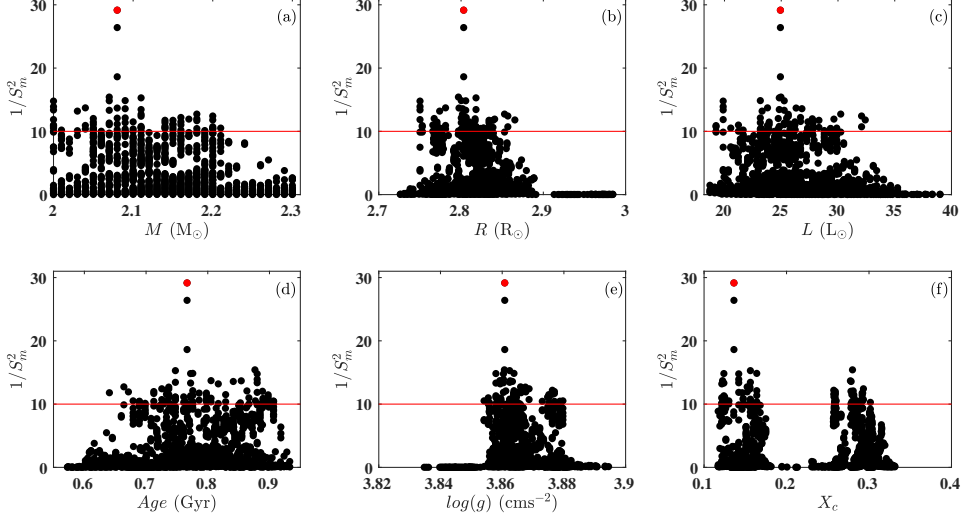


Figure 5. This visualization presents the fitting metric S_m^2 and physical parameters: stellar mass (M), radius (R), luminosity (L), age (Age), gravitational acceleration ($\log g$), and central hydrogen abundance (X_c) with a red horizontal line marking the threshold $S_m^2 = 0.10$, where black dots indicate the minimum S_m^2 for each model while the red dot identifies the minimum S_m^2 of the best-fitting model (Model A3).

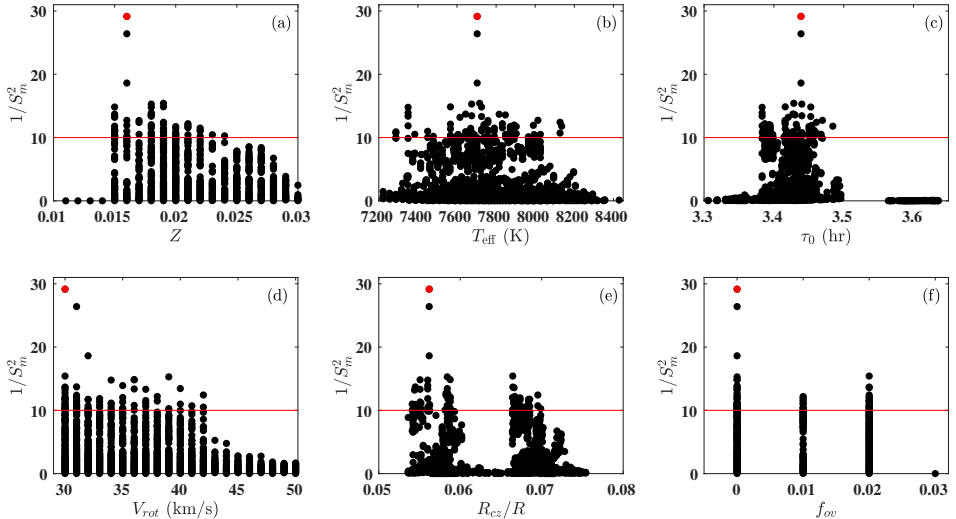


Figure 6. This visualization presents the fitting results S_m^2 alongside key physical parameters: metallicity (Z), effective temperature (T_{eff}), acoustic radius (τ_0), stellar rotation velocity (V_{rot}), convective-core-to-stellar-radius ratio (R_{cz}/R), and overshooting parameter (f_{ov}). A red horizontal line marks the threshold $S_m^2 = 0.10$. Black dots denote the minimum S_m^2 for each model, while a red dot identifies the minimum S_m^2 for the best-fitting model (Model A3).

Figures 5 (a)–(c) display the variation of S_m^2 versus stellar mass (M), radius (R), and luminosity (L). These parameters demonstrate excellent convergence with best-fit values $M = 2.08^{+0.13} M_\odot$, $R = 2.80^{+0.07} R_\odot$, and $L = 24.93^{+7.47} L_\odot$. Meanwhile, Figures 5 (d)–(f) show S_m^2 as functions of age (Age), gravitational acceleration ($\log g$), and central hydrogen abundance (X_c). The parameters age and gravitational acceleration exhibit tight constraints: Age = $0.7664^{+0.1402}_{-0.1258}$ Gyr and $\log g = 3.8608^{+0.0189}_{-0.0067}$ cm s^{-2} . In contrast, the central hydrogen abundance spans a broader range $X_c = 0.1362^{+0.1655}_{-0.0148}$.

Table 4. Comparisons between model frequencies of best-fitting model (Model A3) and observations.

ID	F_{obs} (μHz)	F_{mod} (μHz)	(ℓ, n_p, n_g, m)	$ F_{\text{obs}} - F_{\text{mod}} $ (μHz)
F_{22}	109.4199	109.3071	(0, 0, 0, 0)	0.1128
F_1	140.1847	139.7799	(0, 1, 0, 0)	0.4048
F_2	131.3715	131.2754	(2, 1, -3, 1)	0.0961
F_7	147.5550	147.4214	(3, 1, -3, 0)	0.1336
F_6	125.3907	125.5038	(3, 1, -5, 2)	0.1131
F_3	138.8162	138.6726	(3, 1, -4, -1)	0.1436
F_{13}	106.2529	106.3081	(3, 0, -6, -2)	0.0481

NOTE— F_{obs} is the observed frequency. F_{mod} is the model frequency. (ℓ, n_p, n_g, m) are the spherical harmonic degree, the radial orders in the p-mode propagation zone, the radial orders in the g-mode propagation zone, and the azimuthal number of the model frequency.

Table 5. Fundamental parameters of the component B of DG Leo.

Parameters	Single-star Models
Z	$0.015 - 0.024$ ($0.016^{+0.008}_{-0.001}$)
M (M_{\odot})	$2.00 - 2.21$ ($2.08^{+0.13}_{-0.08}$)
V_{rot} (km s^{-1})	$30 - 42$ (30^{+12}_{-0})
T_{eff} (K)	$7287 - 8135$ (7703^{+432}_{-415})
$\log(g)$ (cm s^{-2})	$3.8541 - 3.8797$ ($3.8608^{+0.0189}_{-0.0067}$)
R (R_{\odot})	$2.75 - 2.87$ ($2.80^{+0.07}_{-0.05}$)
L (L_{\odot})	$19.26 - 32.40$ ($24.93^{+7.47}_{-5.67}$)
τ_0 (hr)	$3.3832 - 3.4844$ ($3.4388^{+0.0456}_{-0.0556}$)
X_c	$0.1214 - 0.3017$ ($0.01362^{+0.1655}_{-0.0148}$)
R_{cz}/R	$0.0541 - 0.0699$ ($0.0562^{+0.0137}_{-0.0021}$)
Age (Gyr)	$0.6406 - 0.9066$ ($0.7664^{+0.1402}_{-0.1258}$)

NOTE— V_{rot} denotes the rotation velocity. τ_0 is the acoustic radius. X_c is the central hydrogen abundance.

Figures 6 (a)–(c) depict the variation of S_m^2 with metallicity (Z), effective temperature (T_{eff}), and acoustic radius (τ_0). Excellent convergence is observed for metallicity and acoustic radius (τ_0) with best-fit values $Z = 0.016^{+0.008}_{-0.001}$ and $\tau_0 = 3.4388^{+0.0456}_{-0.0556}$ hr, while the effective temperature shows a broader distribution $T_{\text{eff}} = 7703^{+432}_{-415}$ K. Meanwhile, Figures 6 (d)–(f) present S_m^2 as functions of rotation velocity (V_{rot}), convective-core-to-stellar-radius ratio (R_{cz}/R), and overshooting parameter (f_{ov}). All three parameters exhibit good convergence: $V_{\text{rot}} = 30^{+12}_{-0}$ km s^{-1} , $R_{\text{cz}}/R = 0.0562^{+0.0137}_{-0.0021}$, and $f_{\text{ov}} = 0.00 - 0.02$.

Table 4 presents a comparison between the observed frequencies and those of the best-fitting model (Model A3). Based on this comparison, F_{22} and F_1 are identified as the fundamental radial mode and the first radial overtone, respectively. F_2 is classified as a quadrupole mode, while F_3 , F_6 , and F_7 are recognized as octupole modes. Although F_{13} does not match any f-mode predicted by the model, it coincides with a g-mode of degree $\ell = 3$. We therefore identify F_{13} as a low-order g-mode with $\ell = 3$. The asteroseismically derived parameters of component B, which are in good agreement with the light curve modeling results, are listed in Column 2 of Table 5. These non-radial modes provide crucial constraints on the internal structure of component B in DG Leo.

5. DISCUSSION AND CONCLUSIONS

The hierarchical and spectroscopic triple system DG Leo, consisting of an inner binary and a distant δ Scuti star, exhibits both ellipsoidal variations and high-amplitude pulsations in its *TESS* light curve. Through modelling of

these ellipsoidal variations, our analysis constrains the inner binary's orbital inclination to $i = 66.87 \pm 0.60^\circ$, which is consistent with prior rough estimates (Barnes et al. 1977; Rosvick & Scarfe 1991a; Frémat et al. 2005). The other orbital parameters are also determined, too. Subsequent in combination our light curve modeling results with spectroscopic results (Lampens et al. 2004; Frémat et al. 2005) yielded dynamically derived stellar parameters: Component Aa has mass $M_1 = 2.258 \pm 0.033 M_\odot$, radius $R_1 = 3.353 \pm 0.015 R_\odot$, and luminosity $L_1 = 25.99 \pm 1.44 L_\odot$; Component Ab shows $M_2 = 2.258 \pm 0.033 M_\odot$, $R_2 = 3.263 \pm 0.025 R_\odot$, $L_2 = 24.48 \pm 1.67 L_\odot$; while component B exhibits $M_B = 2.39 \pm 0.40 M_\odot$, $R_B = 2.95 \pm 0.50 R_\odot$, $L_B = 26.05 \pm 8.42 L_\odot$. When compared with the results obtained using the evolutionary method described in Frémat et al. (2005), the radii ($R_1 = 2.96 \pm 0.2 R_\odot$, $R_2 = 2.94 \pm 0.2 R_\odot$) of the two components of the inner binary are similar to our results, but the masses ($M_1 = 2.0 \pm 0.2 M_\odot$, $M_2 = 2.0 \pm 0.2 M_\odot$) are somewhat smaller. The combination of light curve modeling and spectroscopic results reveals further: i) the inner binary is a detached system comprising two late A-type components that have low Roche lobe filling factors and similar physical parameters; ii) the parameters of component B are slightly larger than those of the inner binary system, and are consistent with them within uncertainties. Therefore, it may be concluded that the three stars in DG Leo have similar physical parameters, indicating that they are at a similar evolutionary stage and have undergone coeval evolution.

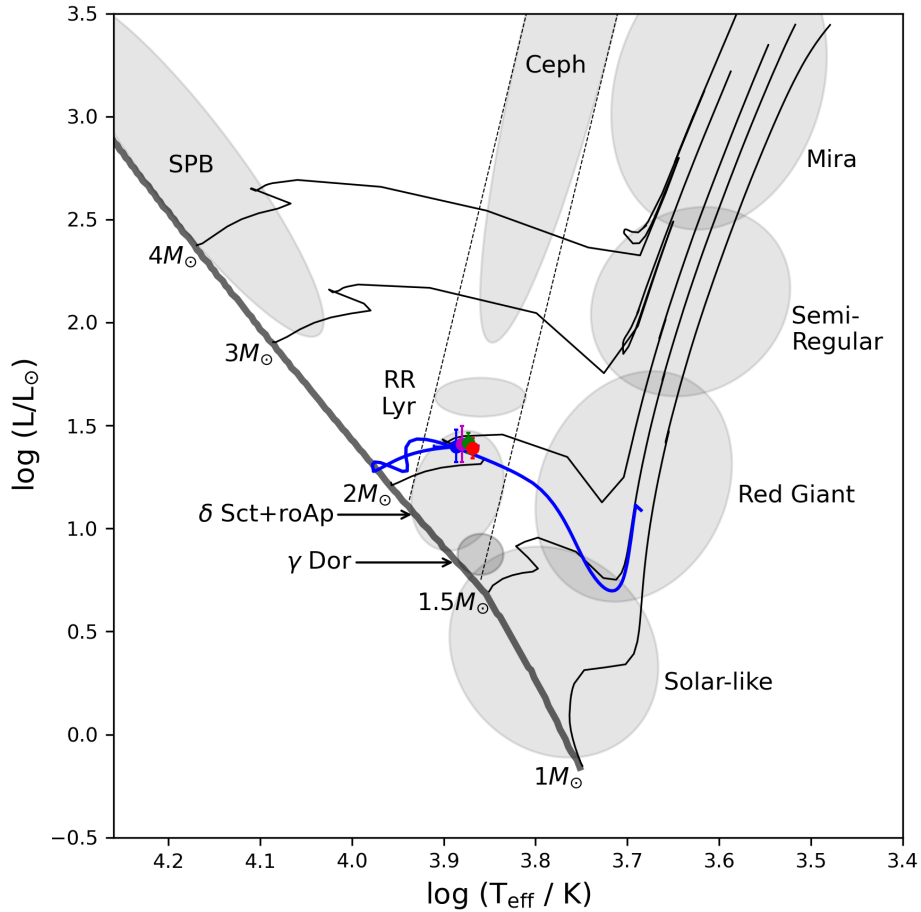


Figure 7. The H-R diagram for DG Leo displays the positions of all three stellar components. The inner binary components are represented by a green dot (Aa) and a red dot (Ab), respectively. Component B's location is indicated by a pink dot, with all positions derived from the light curve modeling. Additionally, a blue dot denotes the current evolutionary state of component B according to the best-fitting stellar model (Model A3), while the accompanying curve traces its predicted evolutionary track.

Moreover, no shallow eclipses of the inner binary system were detected in earlier studies (Lampens et al. 2004; Frémat et al. 2005). We also carefully examined the *TESS* light curves from all four sectors and confirm the absence of any

eclipses. This non-detection is well explained by the orbital geometry. The mean orbital inclination obtained from our light curve modeling (see Table 1) is just below the critical inclination of 68.2° required for eclipses to occur, which is estimated from the stellar radii and orbital separation via $\cos i = \frac{R_1+R_2}{a}$. Given that our measured inclination lies slightly below this theoretical threshold, any eclipses would be extremely shallow and undetectable amid the dominant pulsation signal.

After isolating the intrinsic pulsation signal by subtracting the binary model from the original *TESS* light curve, we performed a multiple frequency analysis on the residuals. This revealed seven significant independent frequencies: F_1 , F_2 , F_3 , F_6 , F_7 , F_{13} , and F_{22} . To identify their pulsation modes, we computed the pulsation constant Q for each frequency using the standard relation. Comparison with theoretical models (Fitch 1981) indicates that F_1 and F_{22} are the first-overtone and fundamental radial modes, respectively — a classification further supported by their period ratio of 0.780. Frequencies F_2 , F_3 , and F_7 are identified as non-radial modes with $l = 2$, 3, and 3, respectively, while F_6 and F_{13} are also likely non-radial. Although amplitude variations are present, a search for tidally induced modulations (e.g., frequency splitting or orbital-phase-dependent variations in amplitude or phase) yielded no significant detections. This confirms that the observed pulsations are intrinsic to component B, consistent with Frémat et al. (2005).

To further verify these mode identifications, trace the evolutionary history of the δ Scuti star, and constrain the evolutionary stage of the triple system, we constructed a grid of theoretical models incorporating the dynamically measured parameters. Our asteroseismic modeling confirms F_{22} and F_1 as the fundamental and first-overtone radial modes, respectively; F_2 as a quadrupole ($\ell = 2$) mode; and F_3 , F_6 , F_7 , and F_{13} as octupole ($\ell = 3$) modes—consistent with the earlier identification. The best-fitting model yields the following fundamental parameters for component B: $M = 2.08^{+0.13}_{-0.08} M_\odot$, $R = 2.80^{+0.06}_{-0.05} R_\odot$, $L = 24.92^{+7.47}_{-5.67} L_\odot$, $T_{\text{eff}} = 7703^{+432}_{-415}$ K, and $v \sin i = 30^{+12}_{-0}$ km s $^{-1}$. These asteroseismic results are consistent with both our dynamical solutions and previously reported values for the effective temperature and projected rotation velocity of component B (Frémat et al. 2005, 2004).

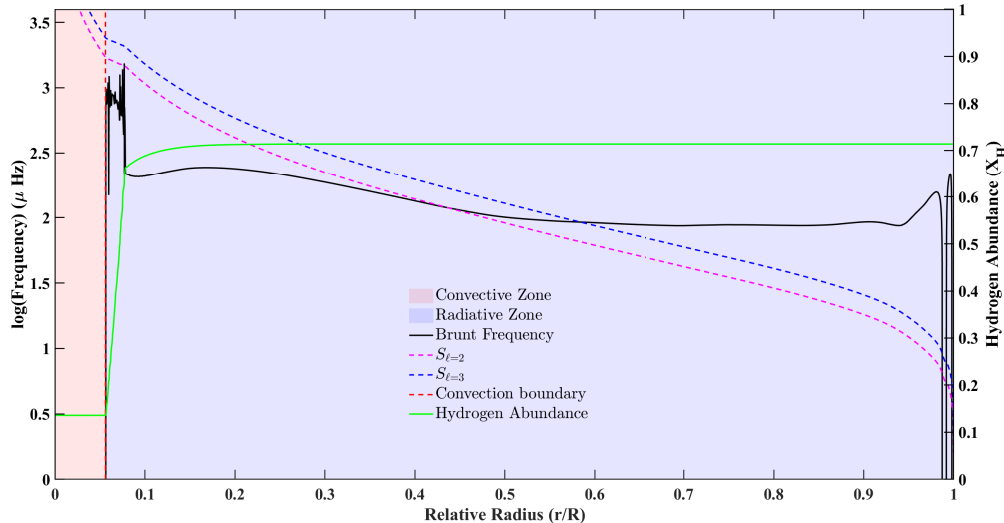


Figure 8. Visualization of the Brunt–Väisälä frequency (N), characteristic acoustic oscillation frequencies (S_ℓ for $\ell = 2, 3$), and hydrogen abundance (X_H) inside the component B. The vertical dashed line indicates the boundary of convective zone ($\nabla_r = \nabla_{ad}$).

Figure 7 presents the H-R diagram for DG Leo, showing positions of all three stellar components. The components of the inner binary, Aa and Ab, are marked by green and red dots, respectively, while component B is indicated by a pink dot. All positions are derived dynamically based on light curve modeling. The blue dot indicates the current evolutionary state of component B derived from theoretical models, consistent with the pink dot within uncertainties. The accompanying blue curve shows its evolutionary track from the pre-main-sequence to the post-main-sequence phase. Component B is thus confirmed to be a post-main-sequence star with an age of $0.7664^{+0.1402}_{-0.1258}$ Gyr. Moreover, we found that components Aa and Ab have evolved slightly more than component B, but they occupy similar positions to each other in the H-R diagram within uncertainties. The near-identical positions of all three components in the

diagram, closely coupled with their similar physical properties (e.g., mass and radius), support their simultaneous formation from the same protostellar environment. Therefore, we conclude that all three components are post-main-sequence stars that share the same age and evolutionary stage. Component B exhibits several characteristics of HADS variables: it is located near the HADS region in the H–R diagram, pulsates predominantly in the first-overtone radial mode, and has a spectral type consistent with late-A type stars (Frémat et al. 2005). However, its observed amplitude is only 0.01 mag (Figure 1)—approximately one-tenth of the typical amplitude for HADS stars—likely due to photometric dilution from the brighter inner binary. We suggest that the component B may be an HADS-like star. Furthermore, the reason for the low amplitude observed in the fundamental mode (F_{22}) remains unclear.

Figure 8 displays radial profiles of the Brunt–Väisälä frequency (N), characteristic acoustic frequencies (S_ℓ for $\ell = 2, 3$), and hydrogen abundance (X_H) in the best-fitting stellar model. Figure 9 reveals that the fundamental radial mode F_{22} and radial first overtone F_1 propagate primarily in the stellar envelope, thereby probing envelope structure. It is also evident that substantial amplitudes of non-radial oscillation modes are present near both the convective core boundary and the envelope. This indicates that these modes exhibit a mixed character. Consequently, non-radial modes provide strong constraints when determining the convective core boundary.

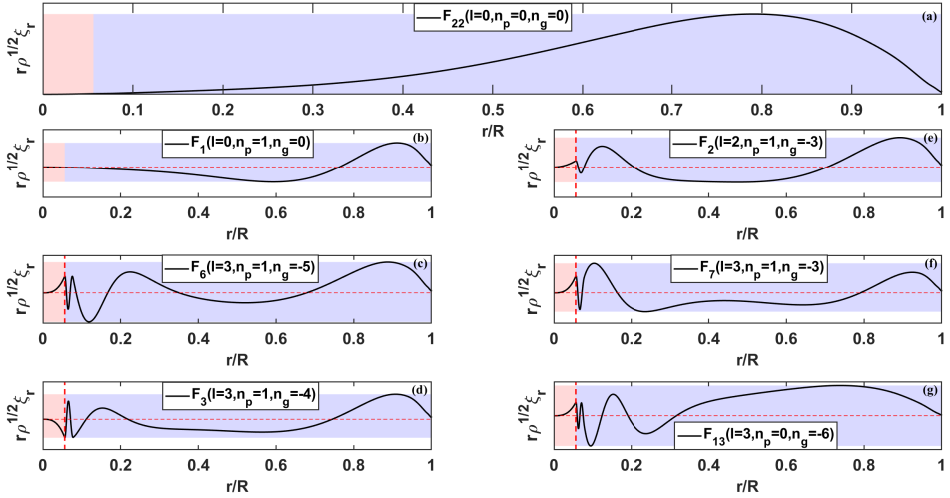


Figure 9. Scaled radial displacement eigenfunctions corresponding to the observed frequencies in the best-fitting model. Panel (a) corresponds to the fundamental radial mode F_{22} ; panel (b) to the first radial overtone mode F_1 ; panels (c), (d), (e), (f), and (g) correspond to the observed frequencies F_6 , F_3 , F_2 , F_7 , and F_{13} , respectively. The vertical red dashed lines mark the boundary of the convective core ($\nabla_r = \nabla_{ad}$).

The acoustic radius τ_0 (sound travel time from center to surface) is defined as (Aerts et al. 2010):

$$\tau_0 = \int_0^R \frac{dr}{c_s} \quad (6)$$

where c_s denotes the adiabatic sound speed. Since c_s in the stellar envelope is significantly lower than in the convective core, τ_0 predominantly characterizes envelope properties. Given that the non-radial modes have substantial amplitudes near the edge of the convective core, we utilize the relative core radius R_{cz}/R to describe the features of the deep interior structure of component B. Consequently, fitting the seven δ Scuti frequencies requires matching both the convective core and stellar envelope in theoretical models to the actual structure of the component B. Figures 6 shows that τ_0 of the candidate models converges well to $3.4388^{+0.0456}_{-0.0556}$ hr and R_{cz}/R of the candidate models converges well to $0.0562^{+0.0137}_{-0.0021}$. This suggests that they are nearly alike in structure.

In summary, DG Leo establishes a hierarchical triple system comprising an inner spectroscopic binary (components Aa and Ab) and a distant component B. All three stars have reached the post-main-sequence stage. This unique configuration provides a natural laboratory for probing coeval stellar evolution, asteroseismology, and dynamical interactions in triple systems. Further investigation of the orbital motion of component B necessitates more precise astrometry

from Gaia (Prusti et al. 2016; Brown et al. 2018) to constrain its long-period orbit. Meanwhile, additional medium- or high-resolution spectral data are essential for resolving non-radial pulsation modes and elemental abundances, as well as for determining more precise physical parameters for component B in the future. This would advance stellar structure and evolution models for DG Leo.

This work is supported by the International Cooperation Projects of the National Key R&D Program (No. 2022YFE0127300), the 2022 CAS “Light of West China” Program, the National Natural Science Foundation of China (No. 12573038), the Postdoctoral Fellowship Program of CPSF under Grant Number GZC20252095, the China Postdoctoral Science Foundation under Grant Number 2025M773194, and the Caiyun Postdoctoral Program in Yunnan Province of China (grant No. C615300504124). The *TESS* data presented in this paper were obtained from the Mikulski Archive for Space Telescopes (MAST) at the Space Telescope Science Institute (STScI). STScI is operated by the Association of Universities for Research in Astronomy, Inc. Support to MAST for these data is provided by the NASA Office of Space Science. Funding for the *TESS* mission is provided by the NASA Explorer Program. The authors are sincerely grateful to an anonymous referee for instructive advice and productive suggestions.

6. APPENDIX INFORMATION

In this Appendix, we present the 84 candidate models generated using the MESA code (see Section 4 for details). The physical parameters of these models—including stellar age, effective temperature, mass, central hydrogen abundance, gravitational acceleration, stellar luminosity, stellar radius, metallicity, stellar rotation velocity, acoustic radius, and convective-core-to-stellar-radius ratio—are listed in Table 6. Among these candidates, Model A3 achieves the global minimum of $S_m^2 = 0.0343$, establishing it as the best-fitting model, which is highlighted by the red dots in Figures 5 and 6.

Table 6. Candidate models with $S_m^2 < 0.10$.

Mode ID	Age (Gyr)	T_{eff} (K)	M (M_{\odot})	X_c	$\log g$ (cm s^{-2})	L (L_{\odot})	R (R_{\odot})	Z	V_{rot} (km/s)	τ_0 (hr)	R_{cz}/R	S_m^2
A1	0.7664	7703	2.08	0.1362	3.8608	24.93	2.80	0.016	31.00	3.4388	0.0562	0.0379
A2	0.7664	7703	2.08	0.1362	3.8608	24.93	2.80	0.016	32.00	3.4388	0.0562	0.0537
A3	0.7664	7703	2.08	0.1362	3.8608	24.93	2.80	0.016	30.00	3.4388	0.0562	0.0343
A4	0.7285	7848	2.11	0.1301	3.8596	27.32	2.83	0.015	31.00	3.4677	0.0560	0.0952
A5	0.7285	7848	2.11	0.1301	3.8596	27.32	2.83	0.015	30.00	3.4677	0.0560	0.0998
A6	0.6406	8135	2.20	0.1463	3.8661	32.40	2.87	0.015	30.00	3.4844	0.0585	0.0847
A7	0.7368	7758	2.11	0.1556	3.8675	25.62	2.80	0.017	30.00	3.4159	0.0583	0.0788
A8	0.7368	7758	2.11	0.1556	3.8675	25.62	2.80	0.017	31.00	3.4159	0.0583	0.0807
A9	0.7610	7755	2.08	0.1249	3.8582	25.76	2.81	0.015	35.00	3.4577	0.0552	0.0975
A10	0.7610	7755	2.08	0.1249	3.8582	25.76	2.81	0.015	34.00	3.4577	0.0552	0.0897
A11	0.6640	8014	2.18	0.1523	3.8660	30.24	2.85	0.016	30.00	3.4696	0.0584	0.0786
A12	0.6714	7991	2.17	0.1523	3.8676	29.64	2.84	0.016	30.00	3.4543	0.0588	0.0838
A13	0.7722	7726	2.07	0.1240	3.8580	25.26	2.81	0.015	36.00	3.4528	0.0551	0.0674
A14	0.7722	7726	2.07	0.1240	3.8580	25.26	2.81	0.015	34.00	3.4528	0.0551	0.0905
A15	0.7722	7726	2.07	0.1240	3.8580	25.26	2.81	0.015	37.00	3.4528	0.0551	0.0750
A16	0.7722	7726	2.07	0.1240	3.8580	25.26	2.81	0.015	35.00	3.4528	0.0551	0.0884
A17	0.8771	7384	2.00	0.1275	3.8541	20.55	2.77	0.017	30.00	3.4215	0.0545	0.0951
A18	0.8529	7479	2.01	0.1217	3.8559	21.65	2.77	0.016	30.00	3.4225	0.0542	0.0980
A19	0.8053	7644	2.04	0.1224	3.8593	23.79	2.78	0.015	32.00	3.4272	0.0545	0.0966
A20	0.8053	7644	2.04	0.1224	3.8593	23.79	2.78	0.015	30.00	3.4272	0.0545	0.0915
A21	0.8053	7644	2.04	0.1224	3.8593	23.79	2.78	0.015	31.00	3.4272	0.0545	0.0729
A22	0.8170	7615	2.03	0.1215	3.8594	23.31	2.77	0.015	31.00	3.4205	0.0544	0.0990
A23	0.8170	7615	2.03	0.1215	3.8594	23.31	2.77	0.015	30.00	3.4205	0.0544	0.0758
A24	0.8667	7450	2.00	0.1214	3.8555	21.23	2.77	0.016	40.00	3.4184	0.0541	0.0910
A25	0.8667	7450	2.00	0.1214	3.8555	21.23	2.77	0.016	39.00	3.4184	0.0541	0.0998
A26	0.8896	7287	2.00	0.1474	3.8595	19.26	2.75	0.019	32.00	3.3836	0.0562	0.0932
A27	0.8896	7287	2.00	0.1474	3.8595	19.26	2.75	0.019	31.00	3.3836	0.0562	0.0917
A28	0.8896	7287	2.00	0.1474	3.8595	19.26	2.75	0.019	30.00	3.3836	0.0562	0.0934

Continued

Table 6 – continued

Mode ID	Age (Gyr)	T_{eff} (K)	M (M_{\odot})	X_c	$\log g$ (cms $^{-2}$)	L (L_{\odot})	R (R_{\odot})	Z	V_{rot} (km/s)	τ_0 (hr)	R_{cz}/R	S_m^2
A29	0.8896	7287	2.00	0.1474	3.8595	19.26	2.75	0.019	33.00	3.3836	0.0562	0.0921
A30	0.7670	7628	2.09	0.1571	3.8649	23.86	2.80	0.018	30.00	3.4144	0.0581	0.0994
A31	0.8801	7350	2.00	0.1420	3.8604	19.88	2.75	0.018	33.00	3.3832	0.0560	0.0843
A32	0.8801	7350	2.00	0.1420	3.8604	19.88	2.75	0.018	36.00	3.3832	0.0560	0.0748
A33	0.8801	7350	2.00	0.1420	3.8604	19.88	2.75	0.018	35.00	3.3832	0.0560	0.0719
A34	0.8801	7350	2.00	0.1420	3.8604	19.88	2.75	0.018	34.00	3.3832	0.0560	0.0677
A35	0.7757	7567	2.09	0.1639	3.8638	23.16	2.80	0.019	31.00	3.4162	0.0588	0.0879
A36	0.7757	7567	2.09	0.1639	3.8638	23.16	2.80	0.019	35.00	3.4162	0.0588	0.0965
A37	0.7757	7567	2.09	0.1639	3.8638	23.16	2.80	0.019	30.00	3.4162	0.0588	0.0825
A38	0.7757	7567	2.09	0.1639	3.8638	23.16	2.80	0.019	36.00	3.4162	0.0588	0.0673
A39	0.7475	7675	2.11	0.1562	3.8624	24.83	2.82	0.018	39.00	3.4400	0.0584	0.0654
A40	0.7475	7675	2.11	0.1562	3.8624	24.83	2.82	0.018	36.00	3.4400	0.0584	0.0927
A41	0.7475	7675	2.11	0.1562	3.8624	24.83	2.82	0.018	40.00	3.4400	0.0584	0.0744
A42	0.7475	7675	2.11	0.1562	3.8624	24.83	2.82	0.018	37.00	3.4400	0.0584	0.0941
A43	0.6892	7994	2.20	0.2590	3.8787	29.35	2.82	0.020	30.00	3.3983	0.0677	0.0956
A44	0.7629	7689	2.14	0.2583	3.8730	24.76	2.80	0.023	31.00	3.3888	0.0671	0.0958
A45	0.6790	8026	2.21	0.2602	3.8797	29.89	2.83	0.020	42.00	3.3985	0.0679	0.0951
A46	0.7369	7791	2.16	0.2589	3.8751	26.21	2.81	0.022	30.00	3.3910	0.0672	0.0907
A47	0.7369	7791	2.16	0.2589	3.8751	26.21	2.81	0.022	32.00	3.3910	0.0672	0.0980
A48	0.7369	7791	2.16	0.2589	3.8751	26.21	2.81	0.022	31.00	3.3910	0.0672	0.0870
A49	0.7125	7892	2.18	0.2592	3.8769	27.74	2.82	0.021	30.00	3.3946	0.0673	0.0958
A50	0.7125	7892	2.18	0.2592	3.8769	27.74	2.82	0.021	31.00	3.3946	0.0673	0.0835
A51	0.7125	7892	2.18	0.2592	3.8769	27.74	2.82	0.021	32.00	3.3946	0.0673	0.0856
A52	0.6889	7995	2.20	0.2592	3.8790	29.34	2.82	0.020	31.00	3.3965	0.0675	0.0962
A53	0.7475	7760	2.15	0.2578	3.8748	25.70	2.80	0.022	30.00	3.3870	0.0667	0.0900
A54	0.7475	7760	2.15	0.2578	3.8748	25.70	2.80	0.022	37.00	3.3870	0.0667	0.0900
A55	0.6986	7965	2.19	0.2582	3.8787	28.80	2.82	0.020	32.00	3.3929	0.0669	0.0988
A56	0.7331	7832	2.16	0.2573	3.8763	26.70	2.81	0.021	37.00	3.3869	0.0667	0.0865
A57	0.7331	7832	2.16	0.2573	3.8763	26.70	2.81	0.021	38.00	3.3869	0.0667	0.0820
A58	0.7987	7755	2.15	0.3017	3.8649	26.22	2.84	0.024	30.00	3.4404	0.0699	0.0973
A59	0.7987	7755	2.15	0.3017	3.8649	26.22	2.84	0.024	31.00	3.4404	0.0699	0.0969
A60	0.7860	7903	2.15	0.2923	3.8642	28.32	2.84	0.020	30.00	3.4530	0.0685	0.0852
A61	0.7860	7903	2.15	0.2923	3.8642	28.32	2.84	0.020	31.00	3.4530	0.0685	0.0941
A62	0.7978	7873	2.14	0.2917	3.8637	27.80	2.83	0.020	30.00	3.4502	0.0684	0.0960
A63	0.7978	7873	2.14	0.2917	3.8637	27.80	2.83	0.020	33.00	3.4502	0.0684	0.0878
A64	0.7978	7873	2.14	0.2917	3.8637	27.80	2.83	0.020	34.00	3.4502	0.0684	0.0945
A65	0.7978	7873	2.14	0.2917	3.8637	27.80	2.83	0.020	31.00	3.4502	0.0684	0.0925
A66	0.7978	7873	2.14	0.2917	3.8637	27.80	2.83	0.020	32.00	3.4502	0.0684	0.0851
A67	0.9066	7605	2.05	0.2857	3.8633	23.21	2.78	0.020	32.00	3.3981	0.0667	0.0958
A68	0.9066	7605	2.05	0.2857	3.8633	23.21	2.78	0.020	34.00	3.3981	0.0667	0.0988
A69	0.9066	7605	2.05	0.2857	3.8633	23.21	2.78	0.020	33.00	3.3981	0.0667	0.0955
A70	0.7255	8127	2.20	0.2932	3.8687	32.08	2.86	0.019	42.00	3.4610	0.0695	0.0805
A71	0.7255	8127	2.20	0.2932	3.8687	32.08	2.86	0.019	41.00	3.4610	0.0695	0.0933
A72	0.8635	7747	2.08	0.2808	3.8612	25.48	2.80	0.019	30.00	3.4321	0.0666	0.0827
A73	0.8290	7879	2.10	0.2792	3.8638	27.35	2.81	0.018	30.00	3.4333	0.0667	0.0870
A74	0.8290	7879	2.10	0.2792	3.8638	27.35	2.81	0.018	31.00	3.4333	0.0667	0.0965
A75	0.8764	7716	2.07	0.2800	3.8607	24.98	2.80	0.019	30.00	3.4285	0.0664	0.0649
A76	0.8413	7847	2.09	0.2783	3.8633	26.82	2.80	0.018	30.00	3.4303	0.0666	0.0737
A77	0.8846	7701	2.06	0.2825	3.8650	24.43	2.78	0.019	40.00	3.3988	0.0667	0.0999
A78	0.8542	7816	2.08	0.2775	3.8626	26.31	2.80	0.018	30.00	3.4283	0.0665	0.0731
A79	0.8979	7670	2.05	0.2816	3.8646	23.94	2.77	0.019	39.00	3.3947	0.0666	0.0973
A80	0.8979	7670	2.05	0.2816	3.8646	23.94	2.77	0.019	36.00	3.3947	0.0666	0.0997
A81	0.8979	7670	2.05	0.2816	3.8646	23.94	2.77	0.019	37.00	3.3947	0.0666	0.0903

Continued

Table 6 – continued

Mode ID	Age (Gyr)	T_{eff} (K)	M (M_{\odot})	X_c	$\log g$ (cms $^{-2}$)	L (L_{\odot})	R (R_{\odot})	Z	V_{rot} (km/s)	τ_0 (hr)	R_{cz}/R	S_m^2
A82	0.8979	7670	2.05	0.2816	3.8646	23.94	2.77	0.019	38.00	3.3947	0.0666	0.0872
A83	0.8887	7738	2.05	0.2781	3.8657	24.74	2.77	0.018	34.00	3.3930	0.0664	0.0996
A84	0.8887	7738	2.05	0.2781	3.8657	24.74	2.77	0.018	35.00	3.3930	0.0664	0.0831

V_{rot} is the rotation velocity. τ_0 is the acoustic radius. X_c is the central hydrogen abundance.

REFERENCES

- Aerts, C., Christensen-Dalsgaard, J., & Kurtz, D. W. 2010, *Asteroseismology* (Springer), doi: [10.1007/978-1-4020-5803-5](https://doi.org/10.1007/978-1-4020-5803-5)
- Antonello, E., & Mantegazza, L. 1982, Information Bulletin on Variable Stars, 2152, 1
- Asplund, M., Grevesse, N., Sauval, A. J., & Scott, P. 2009, *ARA&A*, 47, 481, doi: [10.1146/annurev.astro.46.060407.145222](https://doi.org/10.1146/annurev.astro.46.060407.145222)
- Baker, N., & Kippenhahn, R. 1965, *ApJ*, 142, 868, doi: [10.1086/148359](https://doi.org/10.1086/148359)
- Barnes, III, T. G., Fekel, F. C., & Moffett, T. J. 1977, *PASP*, 89, 658, doi: [10.1086/130203](https://doi.org/10.1086/130203)
- Böhm-Vitense, E. 1958, *ZA*, 46, 108
- Borucki, W. J., Koch, D., Basri, G., et al. 2010, *Science*, 327, 977, doi: [10.1126/science.1185402](https://doi.org/10.1126/science.1185402)
- Breger, M. 2000, in *Astronomical Society of the Pacific Conference Series*, Vol. 210, Delta Scuti and Related Stars, ed. M. Breger & M. Montgomery, 3
- Breger, M., Stich, J., Garrido, R., et al. 1993, *A&A*, 271, 482
- Brown, A. G. A., Vallenari, A., Prusti, T., et al. 2018, *A&A*, 616, A1, doi: [10.1051/0004-6361/201833051](https://doi.org/10.1051/0004-6361/201833051)
- Chen, X., Li, Y., & Zhang, X. 2019, *ApJ*, 887, 253, doi: [10.3847/1538-4357/ab585b](https://doi.org/10.3847/1538-4357/ab585b)
- Chen, X., Zhang, X., Li, Y., et al. 2020, *ApJ*, 895, 136, doi: [10.3847/1538-4357/ab8bd2](https://doi.org/10.3847/1538-4357/ab8bd2)
- Chen, X., Ding, X., Cheng, L., et al. 2022, *ApJS*, 263, 34, doi: [10.3847/1538-4365/aca284](https://doi.org/10.3847/1538-4365/aca284)
- Chevalier, C. 1971, *A&A*, 14, 24
- Christensen-Dalsgaard, J. 2008, *Ap&SS*, 316, 113, doi: [10.1007/s10509-007-9689-z](https://doi.org/10.1007/s10509-007-9689-z)
- Claret, A. 2001, *MNRAS*, 327, 989, doi: [10.1046/j.1365-8711.2001.04783.x](https://doi.org/10.1046/j.1365-8711.2001.04783.x)
- Cowley, A. P. 1976, *PASP*, 88, 95, doi: [10.1086/129905](https://doi.org/10.1086/129905)
- Cowley, A. P., & Bidelman, W. P. 1979, *PASP*, 91, 83, doi: [10.1086/130446](https://doi.org/10.1086/130446)
- Danziger, I. J., & Dickens, R. J. 1967, *ApJ*, 149, 55, doi: [10.1086/149231](https://doi.org/10.1086/149231)
- Dziembowski, W. A., & Goode, P. R. 1992, *ApJ*, 394, 670, doi: [10.1086/171621](https://doi.org/10.1086/171621)
- Eggen, O. J. 1979, *ApJS*, 41, 413, doi: [10.1086/190624](https://doi.org/10.1086/190624)
- Elliott, J. E. 1974, *AJ*, 79, 1082, doi: [10.1086/111657](https://doi.org/10.1086/111657)
- ESA, ed. 1997, *ESA Special Publication*, Vol. 1200, The HIPPARCOS and TYCHO catalogues. Astrometric and photometric star catalogues derived from the ESA HIPPARCOS Space Astrometry Mission
- Fekel, Jr., F. C., & Bopp, B. W. 1977, *PASP*, 89, 216, doi: [10.1086/130103](https://doi.org/10.1086/130103)
- Ferguson, J. W., Alexander, D. R., Allard, F., et al. 2005, *ApJ*, 623, 585, doi: [10.1086/428642](https://doi.org/10.1086/428642)
- Fitch, W. S. 1981, *ApJ*, 249, 218, doi: [10.1086/159278](https://doi.org/10.1086/159278)
- Frémat, Y., Lampens, P., & Hensberge, H. 2004, in *Astronomical Society of the Pacific Conference Series*, Vol. 318, Spectroscopically and Spatially Resolving the Components of the Close Binary Stars, ed. R. W. Hilditch, H. Hensberge, & K. Pavlovski, 342–345
- Frémat, Y., Lampens, P., & Hensberge, H. 2005, *MNRAS*, 356, 545, doi: [10.1111/j.1365-2966.2004.08478.x](https://doi.org/10.1111/j.1365-2966.2004.08478.x)
- Freytag, B., Ludwig, H. G., & Steffen, M. 1996, *A&A*, 313, 497
- Grigahcène, A., Dupret, M. A., Gabriel, M., Garrido, R., & Scuflaire, R. 2005, *A&A*, 434, 1055, doi: [10.1051/0004-6361:20041816](https://doi.org/10.1051/0004-6361:20041816)
- Handler, G., Kurtz, D. W., Rappaport, S. A., et al. 2020, *Nature Astronomy*, 4, 684, doi: [10.1038/s41550-020-1035-1](https://doi.org/10.1038/s41550-020-1035-1)
- Hartkopf, W. I., Mason, B. D., McAlister, H. A., et al. 2000, *AJ*, 119, 3084, doi: [10.1086/301402](https://doi.org/10.1086/301402)
- Herwig, F. 2000, *A&A*, 360, 952, doi: [10.48550/arXiv.astro-ph/0007139](https://doi.org/10.48550/arXiv.astro-ph/0007139)
- Hoffleit, D., & Jaschek, C. 1982, *The Bright Star Catalogue: Fourth Revised Edition (Containing data compiled through 1979)* (Springer)
- Iglesias, C. A., & Rogers, F. J. 1996, *ApJ*, 464, 943, doi: [10.1086/177381](https://doi.org/10.1086/177381)
- Kurtz, D. W., Shibahashi, H., Murphy, S. J., Bedding, T. R., & Bowman, D. M. 2015, *MNRAS*, 450, 3015, doi: [10.1093/mnras/stv868](https://doi.org/10.1093/mnras/stv868)
- Kurtz, D. W., Handler, G., Rappaport, S. A., et al. 2020, *MNRAS*, 494, 5118, doi: [10.1093/mnras/staa989](https://doi.org/10.1093/mnras/staa989)

- Lampens, P., Garrido, R., Parrao, L., et al. 2004, in Revista Mexicana de Astronomia y Astrofisica Conference Series, Vol. 21, Revista Mexicana de Astronomia y Astrofisica Conference Series, ed. C. Allen & C. Scarfe, 73–74
- Lampens, P., Frémat, Y., Garrido, R., et al. 2005, A&A, 438, 201, doi: [10.1051/0004-6361:20042335](https://doi.org/10.1051/0004-6361:20042335)
- Lee, J. W., Hong, K., & Kristiansen, M. H. 2019, AJ, 157, 17, doi: [10.3847/1538-3881/aaf0fb](https://doi.org/10.3847/1538-3881/aaf0fb)
- Lenz, P., & Breger, M. 2005, Communications in Asteroseismology, 146, 53, doi: [10.1553/cia146s53](https://doi.org/10.1553/cia146s53)
- Li, P., Liao, W.-P., Qian, S.-B., et al. 2024, ApJ, 977, 3, doi: [10.3847/1538-4357/ad8bc4](https://doi.org/10.3847/1538-4357/ad8bc4)
- Li, T., Bedding, T. R., Huber, D., et al. 2018, MNRAS, 475, 981, doi: [10.1093/mnras/stx3079](https://doi.org/10.1093/mnras/stx3079)
- Li, Y., & Stix, M. 1994, A&A, 286, 815
- Liakos, A., Niarchos, P., Soydugan, E., & Zasche, P. 2012, MNRAS, 422, 1250, doi: [10.1111/j.1365-2966.2012.20704.x](https://doi.org/10.1111/j.1365-2966.2012.20704.x)
- Loumos, G. L., & Deeming, T. J. 1978, Ap&SS, 56, 285, doi: [10.1007/BF01879560](https://doi.org/10.1007/BF01879560)
- Lucy, L. B. 1967, ZA, 65, 89
- Montgomery, M. H., & O'Donoghue, D. 1999, Delta Scuti Star Newsletter, 13, 28
- Netzel, H., & Smolec, R. 2022, MNRAS, 515, 4574, doi: [10.1093/mnras/stac1938](https://doi.org/10.1093/mnras/stac1938)
- Pápics, P. I. 2012, Astronomische Nachrichten, 333, 1053, doi: [10.1002/asna.201211809](https://doi.org/10.1002/asna.201211809)
- Paxton, B., Bildsten, L., Dotter, A., et al. 2011, ApJS, 192, 3, doi: [10.1088/0067-0049/192/1/3](https://doi.org/10.1088/0067-0049/192/1/3)
- Paxton, B., Cantiello, M., Arras, P., et al. 2013, ApJS, 208, 4, doi: [10.1088/0067-0049/208/1/4](https://doi.org/10.1088/0067-0049/208/1/4)
- Paxton, B., Marchant, P., Schwab, J., et al. 2015, ApJS, 220, 15, doi: [10.1088/0067-0049/220/1/15](https://doi.org/10.1088/0067-0049/220/1/15)
- Paxton, B., Schwab, J., Bauer, E. B., et al. 2018, ApJS, 234, 34, doi: [10.3847/1538-4365/aaa5a8](https://doi.org/10.3847/1538-4365/aaa5a8)
- Poretti, E., Suárez, J. C., Niarchos, P. G., et al. 2005, A&A, 440, 1097, doi: [10.1051/0004-6361:20053463](https://doi.org/10.1051/0004-6361:20053463)
- Prusti, T., de Bruijne, J. H. J., Brown, A. G. A., et al. 2016, A&A, 595, A1, doi: [10.1051/0004-6361/201629272](https://doi.org/10.1051/0004-6361/201629272)
- Qian, S. B., Li, L. J., He, J. J., et al. 2018, MNRAS, 475, 478, doi: [10.1093/mnras/stx3185](https://doi.org/10.1093/mnras/stx3185)
- Rappaport, S. A., Kurtz, D. W., Handler, G., et al. 2021, MNRAS, 503, 254, doi: [10.1093/mnras/stab336](https://doi.org/10.1093/mnras/stab336)
- Ricker, G. R., Winn, J. N., Vanderspek, R., et al. 2015, Journal of Astronomical Telescopes, Instruments, and Systems, 1, 014003, doi: [10.1117/1.JATIS.1.1.014003](https://doi.org/10.1117/1.JATIS.1.1.014003)
- Rogers, F. J., & Nayfonov, A. 2002, ApJ, 576, 1064, doi: [10.1086/341894](https://doi.org/10.1086/341894)
- Rosvick, J. M., & Scarfe, C. D. 1991a, PASP, 103, 628, doi: [10.1086/132862](https://doi.org/10.1086/132862)
- . 1991b, MNRAS, 252, 68, doi: [10.1093/mnras/252.1.68](https://doi.org/10.1093/mnras/252.1.68)
- Saio, H. 1981, ApJ, 244, 299, doi: [10.1086/158708](https://doi.org/10.1086/158708)
- Shi, X.-d., Qian, S.-b., & Li, L.-J. 2022, ApJS, 259, 50, doi: [10.3847/1538-4365/ac59b9](https://doi.org/10.3847/1538-4365/ac59b9)
- Shi, X.-d., Qian, S.-b., Li, L.-j., & Liao, W.-p. 2021, MNRAS, 505, 6166, doi: [10.1093/mnras/stab1657](https://doi.org/10.1093/mnras/stab1657)
- Templeton, M., Basu, S., & Demarque, P. 2002, ApJ, 576, 963, doi: [10.1086/341805](https://doi.org/10.1086/341805)
- Van Hamme, W. 1993, AJ, 106, 2096, doi: [10.1086/116788](https://doi.org/10.1086/116788)
- Van Hamme, W., & Wilson, R. E. 2007, ApJ, 661, 1129, doi: [10.1086/517870](https://doi.org/10.1086/517870)
- Wilson, R. E. 1979, ApJ, 234, 1054, doi: [10.1086/157588](https://doi.org/10.1086/157588)
- . 1990, ApJ, 356, 613, doi: [10.1086/168867](https://doi.org/10.1086/168867)
- Wilson., R. E. 2012, AJ, 144, 73, doi: [10.1088/0004-6256/144/3/73](https://doi.org/10.1088/0004-6256/144/3/73)
- Wilson, R. E., & Devinney, E. J. 1971, ApJ, 166, 605, doi: [10.1086/150986](https://doi.org/10.1086/150986)
- Zeng, Q.-H., Liao, W.-P., Qian, S.-B., et al. 2024, ApJ, 975, 249, doi: [10.3847/1538-4357/ad83b2](https://doi.org/10.3847/1538-4357/ad83b2)
- Zhevakin, S. A. 1963, ARA&A, 1, 367, doi: [10.1146/annurev.aa.01.090163.002055](https://doi.org/10.1146/annurev.aa.01.090163.002055)